High Entropy Alloys & Materials
https://doi.org/10.1007/s44210-022-00005-5

ORIGINAL PAPER

$Fe_{30}Co_{40}Mn_{15}Al_{15}$: A Novel Single-Phase B2 Multi-Principal Component Alloy Soft Magnet

Youxiong Ye[1] · Scott D. Lish[1] · Liubin Xu[2] · Si Chen[3] · Yang Ren[3] · Aparna Saksena[4] · Baptiste Gault[4,5] · Markus W. Wittmann[1] · Haixuan Xu[2] · Ian Baker[1]

Received: 24 June 2022 / Accepted: 12 August 2022

Abstract
Soft magnets play a vital role in the efficient energy conversion in a variety of important industries including wide-bandgap semiconductors, electric vehicles, aeronautics and aerospace, particularly at high temperatures. Improving the efficiency of modern power electronics and electrical machines via advanced soft magnets has the potential to significantly contribute to global energy savings, thereby leading to a reduction of the associated carbon footprint. Here, we present microstructural characterization and property measurements on a novel single-phase B2-ordered multi-principal element alloy (MPEA) $Fe_{30}Co_{40}Mn_{15}Al_{15}$ with soft magnetic properties suitable for high-temperature magnetic applications. The MPEA exhibits a high saturation magnetization of 162 $Am^2\ kg^{-1}$, high Curie temperature of 1081 K, low coercivity of 114 A m^{-1}, and high electrical resistivity of 230 μΩ cm. Because of the good thermal stability of the B2 phase, these soft magnetic properties can be retained even after long-term anneals at 873 K, an important attribute for enabling the use of wide-bandgap semiconductors that operate at high temperatures.

Keywords Multi-principal element alloy · B2 ordering · Soft magnetic properties · Thermal stability · ALCHEMI · Density functional theory

Introduction

Soft magnetic materials play a vital role in the efficient operation of modern power electronics and electrical machines (inductors, generators, motors, etc.) for a broad range of applications in wide-bandgap semiconductors, in electric vehicles, and in the aeronautics and aerospace industries, especially at high temperatures [1, 2]. Due to this wide range of applications, improved efficiency of electromagnetic devices has the potential to significantly contribute to global energy savings by as much as 20% and, hence, reduce the carbon footprint [1, 2]. Advanced soft magnetic materials usually require high saturation magnetization (M_s) to increase the range of field amplitudes available for use, low coercivity (H_c) to minimize frequency-independent hysteretic energy loss, high electrical resistivity (ρ) to minimize eddy current loss, high Curie temperature (T_c) and high thermal stability for high-temperature applications. However, traditional soft magnetic materials have shortcomings. For instance, the processing of silicon steels is quite complex and time-consuming; Permalloy (Ni-18% Fe) has low electrical resistivity and, thus, endures high eddy current losses; FeCo–2V alloys also have low electrical resistivity and are expensive because of the high cobalt content; soft ferrites suffer from relatively low magnetization which limits its energy density of inductive elements containing a ferrite core; amorphous and nanocrystalline soft magnets have limited sizes and are thermally unstable which limits high-temperature applications.

✉ Ian Baker
Ian.Baker@dartmouth.edu

1 Thayer School of Engineering, Dartmouth College, Hanover, NH 03755, USA

2 Department of Materials Science and Engineering, The University of Tennessee, Knoxville, TN 37996, USA

3 X-ray Science Division, Argonne National Laboratory, Lemont, IL 60439, USA

4 Max-Planck-Institut für Eisenforschung, Max-Planck-Straße 1, 40237 Düsseldorf, Germany

5 Department of Materials, Royal School of Mines, Imperial College London, Prince Consort Road, London SW7 2BP, UK

Published online: 30 August 2022

The emergence of multi-principal element alloys (MPEAs), including high-entropy alloys (HEAs) and medium-entropy alloys (MEAs), has attracted extensive research attention since 2004 [3, 4]. In contrast to conventional alloys with one principal element, this new class of alloys contains several principal metallic elements in equiatomic or near-equiatomic ratios, and this multi-principal element concept has broadened the composition space for alloy design and offered opportunities for discovery of advanced alloys. MPEAs are usually single-phase solid solutions with simple crystal structures, such as face-centered cubic (FCC) and body-centered cubic (BCC) structures [5–9]. MPEAs have been reported to exhibit exceptional mechanical properties, such as a combination of high strength and ductility [9–12], high fracture toughness [7], high fatigue resistance [13], excellent thermal stability [14, 15] and attractive tribological properties [16, 17]. Beyond mechanical properties, MPEA systems can also exhibit promising soft magnetic properties because of the high flexibility of tuning the chemical compositions and microstructures [18–31]. For example, Zhang et al. synthesized the single-phase FCC $FeCoNiAl_{0.2}Si_{0.2}$ MPEA, which had a saturation magnetization (M_s) of 1.15 T (or ~ 131 $Am^2\ kg^{-1}$) and a coercivity (H_c) of 1400 A m^{-1} [22]. Zuo et al. produced the FeCoNiMnAl MPEA that consisted of a mixture of BCC and B2 (ordered BCC) phases, which exhibited a M_s of ~ 148 $Am^2\ kg^{-1}$ and a H_c of ~ 629 A m^{-1}. They suggested that the Al could suppress the anti-ferromagnetic order associated with Mn in order to favor ferromagnetism [21]. Recently, spinodal decomposition into two coherent FCC phases was shown to lead to an increase of the Curie temperature by 48% and a simultaneous increase of magnetization by 70% in a $Fe_{15}Co_{15}Ni_{20}Mn_{20}Cu_{30}$ MPEA [31]. Almost all the soft magnet MPEAs reported so far were either single-/dual-phase disordered solid solutions (e.g., FCC or BCC) or a mixture of disordered and ordered structures, e.g., FCC or BCC plus B2 or $L2_1$ (a further ordering of the B2 structure) or $L1_2$ (ordered FCC) [18–31]. It has been shown that soft magnetic properties can be improved by increased order in FeCo-based alloys [32–35].

In this study, we present the microstructure, magnetic properties (saturation magnetization, coercivity and Curie temperature) and electrical resistivity of the MPEA $Fe_{30}Co_{40}Mn_{15}Al_{15}$, which has better soft magnetic performance than previously reported MPEAs. The effect of prolonged annealing on microstructural and magnetic stability was also studied with an eye to potential of high-temperature applications.

Methods

Material Preparation

70 g alloy ingots with a nominal atomic composition of $Fe_{30}Co_{40}Mn_{15}Al_{15}$ were prepared by arc melting 99.97% Fe, 99.5% Co, 99.9% Mn, and 99.9% Al pieces under a Ti-gettered high purity argon atmosphere. The ingots were flipped and remelted three times in a water-cooled copper mold to ensure chemical homogeneity. The alloy was eventually cast into ingots with dimension of ~ 40 mm in diameter and ~ 8 mm in thickness. In order to investigate the thermal stability of the MPEA in terms of phase structure and soft magnetic behavior, various heat treatments were conducted on as-cast specimens, including isochronal annealing at 873 K, 1073 K, and 1273 K for 75 h, and isothermal annealing at 873 K for three different times of 150 h, 300 h, and 500 h. All heat treatments were followed by water quenching.

Microstructural Characterization

Crystallographic information for the as-cast and heat-treated specimens was determined using synchrotron X-ray diffraction (XRD) at beamline 11-ID-C (wavelength = 0.1173 Å) at the Advanced Photon Source at Argonne National Laboratory.

Microstructural characterization of the as-cast and heat-treated samples were performed using a Thermo Scientific Helios 5CX Dual Beam scanning electron microscope (SEM) equipped with a back-scattered electron (BSE) detector and energy dispersive X-ray spectrometry (EDS) at an accelerating voltage of 20 kV, and a FEI Tecnai F20 FEG transmission electron microscope (TEM) at an accelerating voltage of 200 kV. Samples for TEM observations were either thinned via twin-jet electropolishing in a Struers TenuPol-5 unit with a solution of 30% nitric acid in methanol at ~ 20 V at a temperature of 253 K, or by focused ion beam (FIB) lift-out technique using the Thermo Scientific Helios.

Atom probe tomography (APT) was performed to analyze the local chemical composition of the sample by employing a local electrode atom probe (LEAP), 5000 XR (Cameca Instrument Inc., Madison, WI, USA). Laser-assisted field evaporation was performed at 50 K by applying a laser pulse energy of 40 pJ at a repetition rate of 125 kHz.

To determine the atomic site occupancy of each element, ALCHEMI (Atom Location by CHanneling Enhanced MIcroanalysis) [36–39] experiments were performed using the FEI Tecnai TEM equipped with Bruker Quantax 200 EDS with XFlash 6T-30. X-ray spectra were collected using the EDS detector under various dynamical (channeling) and kinematical (non-channeling) conditions by tilting the specimen using a low background analytical double tilt holder. Specifically, axial channeling data were obtained directly along the <100> and <110> zone axes; planar channeling conditions were performed from $(00\bar{5})$ to (005) reflections near the above zone axes. Spectra were acquired for 100–200 s to yield similar high counts of ~ 40,000 for the Co-K_α peak. The background was subtracted for subsequent

analyses. As the Fe and Co elements do not have clearly separated K_α emission peaks, i.e., the Fe-K_α peak is superimposed on the Mn-K_β peak, and the Co-K_α peak is superimposed on the Fe-K_β peak, deconvolution analyses with Series fit setting were performed in the Bruker ESPRIT software to separate them (see Fig. S4 in the Supporting Information).

Magnetic and Electrical Property Measurements

Cube-shaped samples for both as-cast and various heat-treated conditions with dimensions of ~ 2.3 mm × 2.3 mm × 2.3 mm were used for magnetic properties measurements on a Lakeshore Instruments 7300 vibrating sample magnetometer (VSM). Magnetization hysteresis loops were performed at room temperature under a maximum applied field of 10 kOe (or ~ 800 kA m^{-1}) with at least three tests for each specimen condition to obtain the saturation magnetization M_s and coercivity H_c. The Curie temperatures T_c of the as-cast and heat-treated specimens were also measured with the VSM from 323 to 1223 K under an applied field of 5 kOe (or ~ 400 kA m^{-1}). The electrical resistivity ρ was measured using sheet samples with thicknesses of ~ 0.5 mm with at least 10 measurements for each condition at room temperature using a Four Point Probe Resistivity system.

First-Principles Calculations

Density functional theory (DFT) calculations were carried out to investigate the magnetic properties of the $Fe_{30}Co_{40}Mn_{15}Al_{15}$ alloy via the Vienna Ab Initio Simulation Package (VASP) [40, 41]. The Perdew–Burke–Ernzerhof (PBE) exchange–correlation functional [42] in the form of projector-augmented wave (PAW) [43] was employed. A supercell size of 4 × 4 × 4 of the B2 conventional cell was adopted in the simulation, resulting in 128 atoms in total. The chemical composition and crystallographic (atomic site occupation of each element) information experimentally obtained from SEM/EDS and ALCHEMI analysis was used as inputs for the ab initio DFT calculations. To better account for the randomness of the atomic-distribution within each type of the lattice sites, the special quasi-random structure (SQS) technique [44] was utilized and three distinguished SQSs were generated with the help of the Monte Carlo code implemented in the Alloy-Theoretic Automated Toolkit [45, 46]. Up to 3rd and 1st nearest neighbor for pairs and triplets were considered in the search of the SQSs, respectively. The ionic positions of each SQS were then optimized until the Hellman–Feynman force on each ion was less than 0.01 eV $Å^{-1}$ while the lattice constant was fixed as the experimental one. The electronic convergence was set to 10^{-6} eV. The energy cut-off of the plane wave basis was tested to be 405 eV. The 2 × 2 × 2 gamma-centered Monkhorst–Pack *k*-point grid was used in the structural optimization while the 4 × 4 × 4 mesh was used in the density of state (DOS) calculation.

Results and Discussion

Microstructures and Thermal Stability

Figure 1a shows synchrotron X-ray diffraction (XRD) patterns of the as-cast $Fe_{30}Co_{40}Mn_{15}Al_{15}$ and a series of heat-treated samples. The as-cast diffraction pattern (black curve) shows superlattice peaks associated with a B2-ordered structure. Dark-field transmission electron microscopy (TEM) imaging using {001} superlattice reflections (Fig. 1b) and the corresponding selected area electron diffraction (SAED) pattern (Fig. 1c) confirm a single B2 phase. The B2 lattice parameter, determined from the synchrotron XRD pattern (Fig. S1a), is 2.8753 ± 0.0002 Å in the as-cast state. The alloy has an average grain size of ~ 250 μm (Fig. 2a). The dark points in the backscattered electron (BSE) images are Al-rich nitride particles, as shown in an enlarged image and its corresponding energy dispersive X-ray spectrometry (EDS) spectrum in Fig. 2b and c. The average volume fraction of the Al-rich nitride particles is determined to be only ~ 0.3%, and, thus, is not considered as a microstructurally relevant factor for influencing the magnetic properties in this study. EDS mapping (Fig. 2d) reveals that all constituent elements are uniformly distributed without micro-scale precipitates (except the scattered Al-rich nitride particles). The measured chemical composition is close to the nominal composition, as summarized in Table 1.

Atom probe tomography (APT) analyses were also employed to further confirm the sub-nanometer-scale compositional homogeneity. As illustrated in Fig. 1f, the elemental maps for the as-cast condition reveal a uniform distribution of the constituents without noticeable segregation across the investigated volume. The chemical composition is consistent with that found via EDS in the scanning electron microscope (SEM), as summarized in Table 1. The slightly lower Al content is likely associated with the aforementioned Al-rich nitride particles, which were not included in the APT investigation. Moreover, the local atomic-distribution randomness was also quantified via frequency distribution analysis (FDA) [47], as displayed in Fig. 1g. It is readily seen that the observed data points overlap extremely well with the binomial distribution, indicative of good chemical homogeneity. The Pearson correlation coefficient μ [47] is also calculated, which lies between 0 and 1 (where 0 indicates a random distribution and 1 indicates segregation). The value for each element is close to 0 (the inset of Fig. 1g), suggesting a homogenous distribution of the alloying elements. In summary, multi-scale microstructure

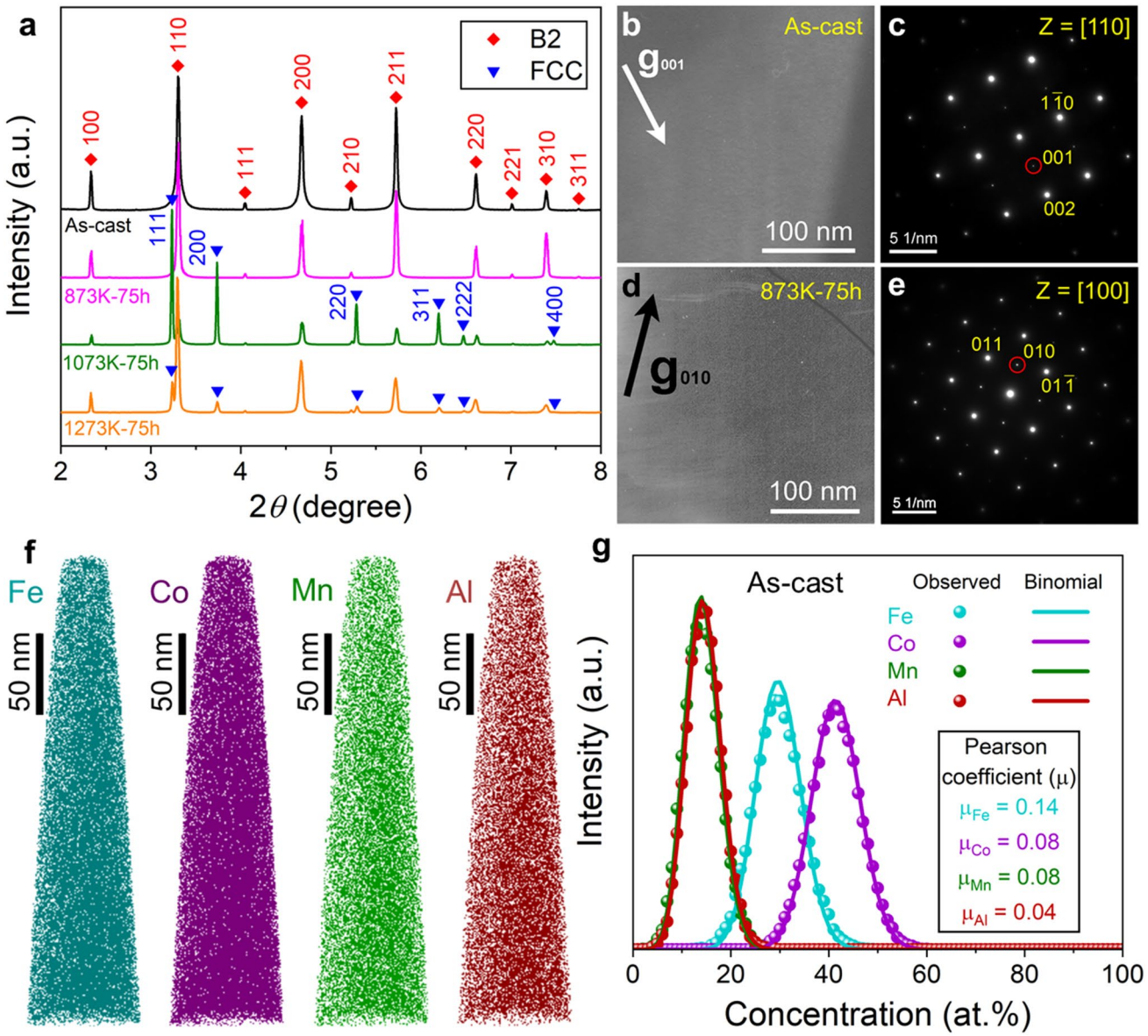

Fig. 1 Phase and microstructural information of $Fe_{30}Co_{40}Mn_{15}Al_{15}$. **a** Synchrotron XRD patterns of $Fe_{30}Co_{40}Mn_{15}Al_{15}$ in the as-cast state and after heat-treatments at 873 K, 1073 K and 1273 K for 75 h. **b–e** Dark-field TEM images and the corresponding SAED patterns of as-cast and 873 K heat-treated specimens. The zone axes and diffraction vectors g used to obtain the images are indicated. **f** APT reconstructions and **g** frequency distribution analysis (FDA) of the constituent elements for as-cast specimen, with inset of (**g**) showing the Pearson correlation coefficient μ

characterizations via combined synchrotron XRD, dark-field TEM image/SAED, SEM/EDS, and APT confirm a single-phase B2-ordered structure with a homogenous distribution of alloying elements for the MPEA.

Although MPEAs usually exhibit disordered solid-solution structures, a single-phase B2-ordered phase was obtained for $Fe_{30}Co_{40}Mn_{15}Al_{15}$. To understand the phase formation of the B2 structure, several physical parameters were calculated according to the phase selection criteria proposed by Zhang et al. [48] and Guo et al. [49]: atomic size difference (δ), mixing enthalpy (ΔH_{mix}), and a specially defined parameter Ω. Specifically, $\delta = 5.4\%$, $\Delta H_{mix} = -9.93$ kJ mol^{-1}, $\Omega = 1.76$ were determined for current MPEA. Details about calculations of these parameters are described in Note S1 in the Supporting Information. Figure S2 shows the typical δ-ΔH_{mix} and δ-Ω plots adapted from [48, 49] for a variety of MPEAs and current $Fe_{30}Co_{40}Mn_{15}Al_{15}$ alloy. It is readily seen that the $Fe_{30}Co_{40}Mn_{15}Al_{15}$ alloy is located in the IM (intermetallic) region in both plots. Therefore, our experimental

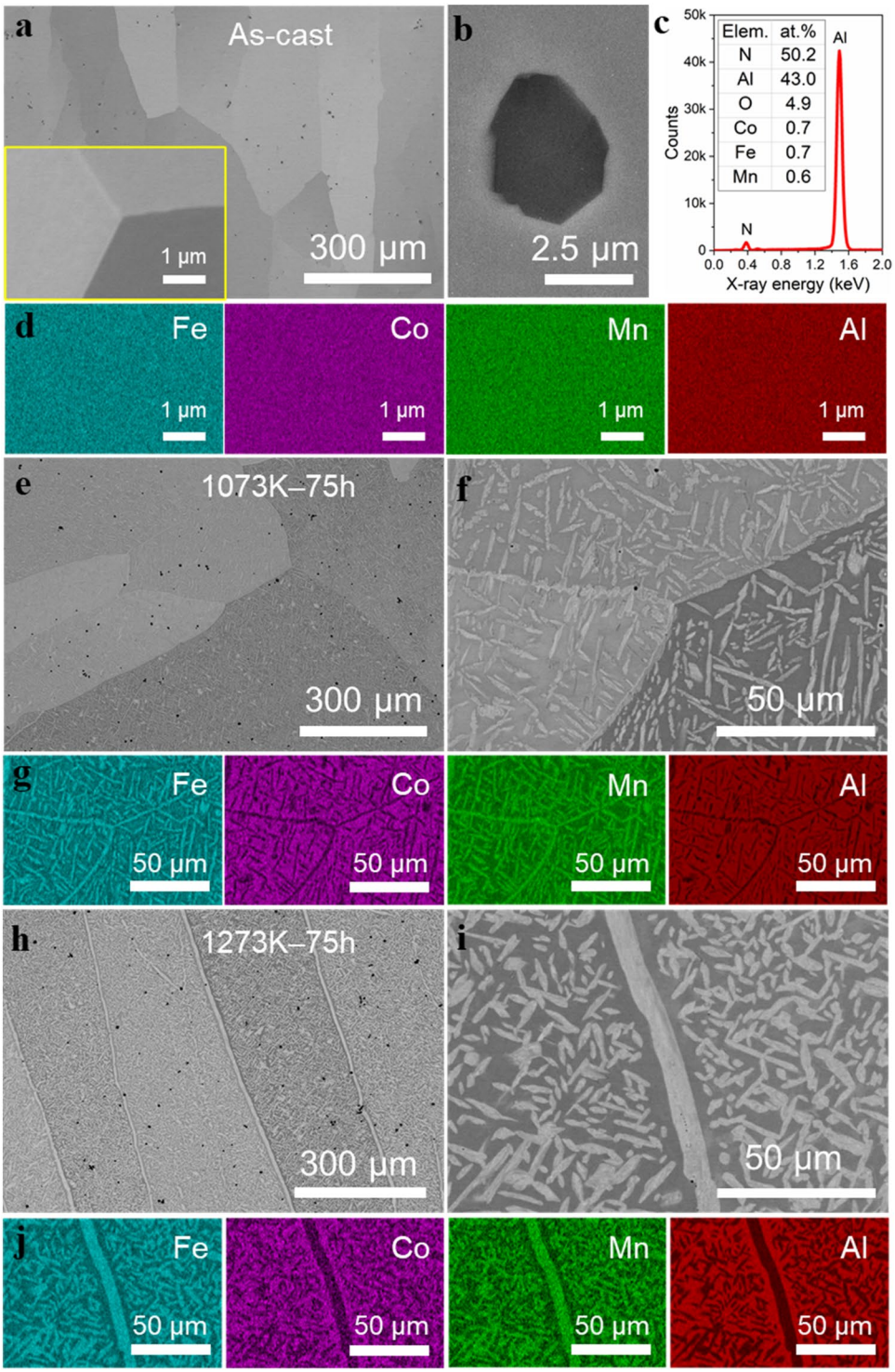

Fig. 2 Microstructure and phase information for as-cast and annealed specimens. **a** Back-scattered electron (BSE) images of the as-cast sample, with the lower left inset showing a higher magnification image. **b**, **c** BSE image and the corresponding EDS spectrum of an Al-rich nitride particle. **d** The corresponding EDS mappings of the four constituent elements of the inset of (**a**). **e**, **h** BSE image, **f**, **i** enlarged views of BSE images showing FCC phase distributed within grain interiors and along grain boundaries, and **g**, **j** corresponding EDS mappings of the four constituent elements of (**f**, **i**) for 1073 K/75 h and 1272 K/75 h heat-treated samples, respectively

observations of forming a B2-ordered phase (synchrotron XRD and TEM in Fig. 1) are consistent with the phase selection criteria proposed by Zhang et al. [48] and Guo et al. [49].

To investigate the microstructural stability and the occurrence of any phase transformations, the as-cast MPEA was heat-treated at 873 K, 1073 K, and 1273 K for 75 h. The synchrotron XRD pattern of the 873 K annealed specimen (pink curve in Fig. 1a) shows that the MPEA is still a single-phase B2 structure with a slightly smaller lattice parameter of 2.8744 ± 0.0002 Å at this temperature. This is corroborated by the TEM dark-field image obtained with a {010} superlattice reflection and the corresponding SAED pattern, see Fig. 1d and e. Upon increasing the

Table 1 Chemical compositions (in at.%) for various specimens determined by SEM/EDS

	Fe	Co	Mn	Al
As-cast	31.3 ± 0.2	39.8 ± 0.2	14.6 ± 0.1	14.3 ± 0.2
As-cast (APT)	31.7 ± 0.5	40.7 ± 0.4	14.2 ± 0.3	13.5 ± 0.3
873 K–75 h	31.2 ± 0.4	39.7 ± 0.1	14.7 ± 0.2	14.4 ± 0.1
1073 K–75 h (B2)	30.7 ± 0.5	42.0 ± 0.3	11.5 ± 0.2	15.8 ± 0.3
1073 K–75 h (FCC)	41.8 ± 0.2	32.2 ± 0.7	22.2 ± 0.7	3.8 ± 0.3
1273 K–75 h (B2)	26.0 ± 0.1	41.7 ± 0.2	12.2 ± 0.1	20.2 ± 0.3
1273 K–75 h (FCC)	37.6 ± 0.3	37.2 ± 0.3	17.5 ± 0.2	7.7 ± 0.1

The standard deviations are determined based on EDS counting statistics. The composition for as-cast condition measured via APT is also included

annealing temperatures to either 1073 K (green curve) or 1273 K (orange curve), extra peaks associated with an additional FCC phase are readily identified in the synchrotron XRD patterns (marked by blue triangles for green and orange curves in Fig. 1a). These rod/plate-like FCC precipitates are uniformly distributed in the grain interiors, as well as distributed along the grain boundaries, as shown in Fig. 2e–j. The corresponding EDS mappings (Fig. 2g, j) for both 1073 K and 1273 K annealed specimens indicate that the FCC phase is enriched with Fe and Mn whereas the B2 matrix is enriched with Co and Al. The relatively large difference in lattice parameters of the FCC phase (3.5966 and 3.5908 Å in Fig. S1c, d) in the 1073 K and 1273 K annealed specimens can be associated with their different compositions (Table 1). Further anneals at 873 K for up to 500 h were also performed and it was observed from both synchrotron XRD data and BSE images (Fig. 3) that only a small volume fraction (~ 1.5%) of FCC precipitates with sizes of 100–300 nm were present after the 500 h anneal, indicating the good thermal stability of the alloy. In general, it can be concluded that $Fe_{30}Co_{40}Mn_{15}Al_{15}$ exhibits high thermal stability up to 873 K, but phase separation takes place after heat treatment at higher temperatures (1073 K and 1273 K). Note that these anneals did not produce any significant change in grain size, presumably because the as-cast grain size was so large (250 µm).

Atomic Site Occupancy of Alloying Elements

The long-range atomic order can be revealed by the atomic site occupancy of each element. Fundamental knowledge of the atomic site occupancy is essential to understand the role of the alloying elements on a variety of alloy properties, including the magnetic properties. The method of ALCHEMI (Atom Location by CHanneling Enhanced MIcroanalysis) [36–39], a TEM technique based on the orientation-dependence of characteristic X-ray emissions of alloying elements, was employed to determine the site occupancy preference of the MPEA. The site occupancy preference of alloying elements was analyzed and quantified, as summarized in Figs. 4 and S3. The detailed ALCHEMI analysis is described in Note S2. It is readily observed that the normalized intensities of Co-K_α, Fe-K_α, and Mn-K_α behave similarly, i.e., they remain almost constant from kinematical to dynamical channeling conditions, while the Al-K_α X-ray intensity is enhanced significantly for either axial channeling and planar channeling conditions (Figs. 4a-e, S3). Since it is impossible for all Co, Fe, and Mn atoms (~ 85 at.% together) to occupy on one sublattice site in the B2 lattice, it is inferred that Co, Fe, and Mn atoms tend to partition between the two sublattice site, whereas the Al atoms preferentially reside on one site (Al-site) in the B2 lattice.

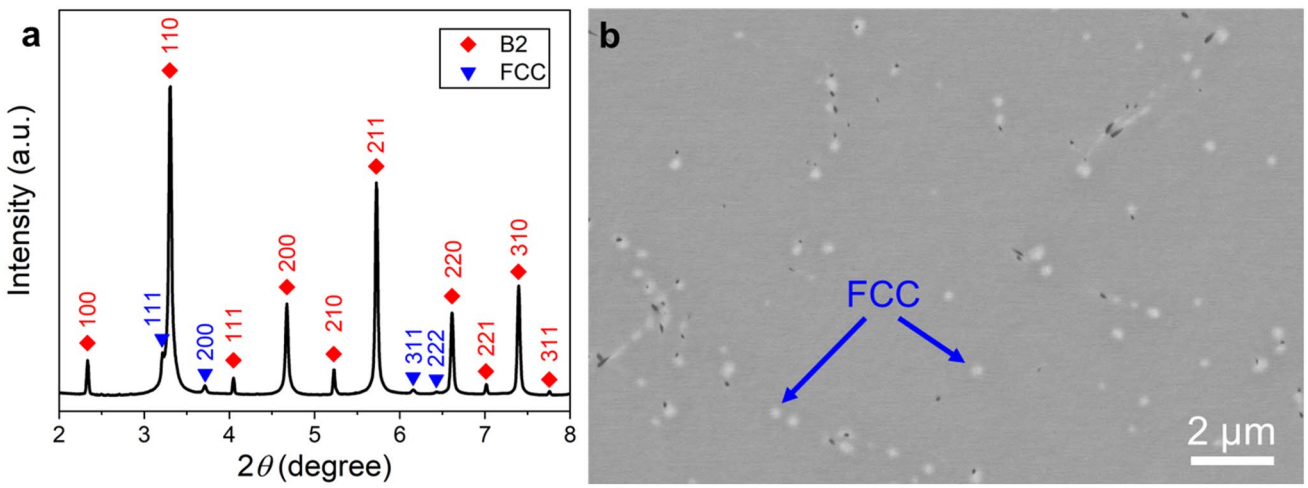

Fig. 3 Phase and microstructural information of 873 K/500 h annealed $Fe_{30}Co_{40}Mn_{15}Al_{15}$. **a** Synchrotron XRD pattern and **b** BSE image showing B2 matrix and FCC precipitates. The FCC precipitates have sizes of 100–300 nm with ~ 1.5% fraction

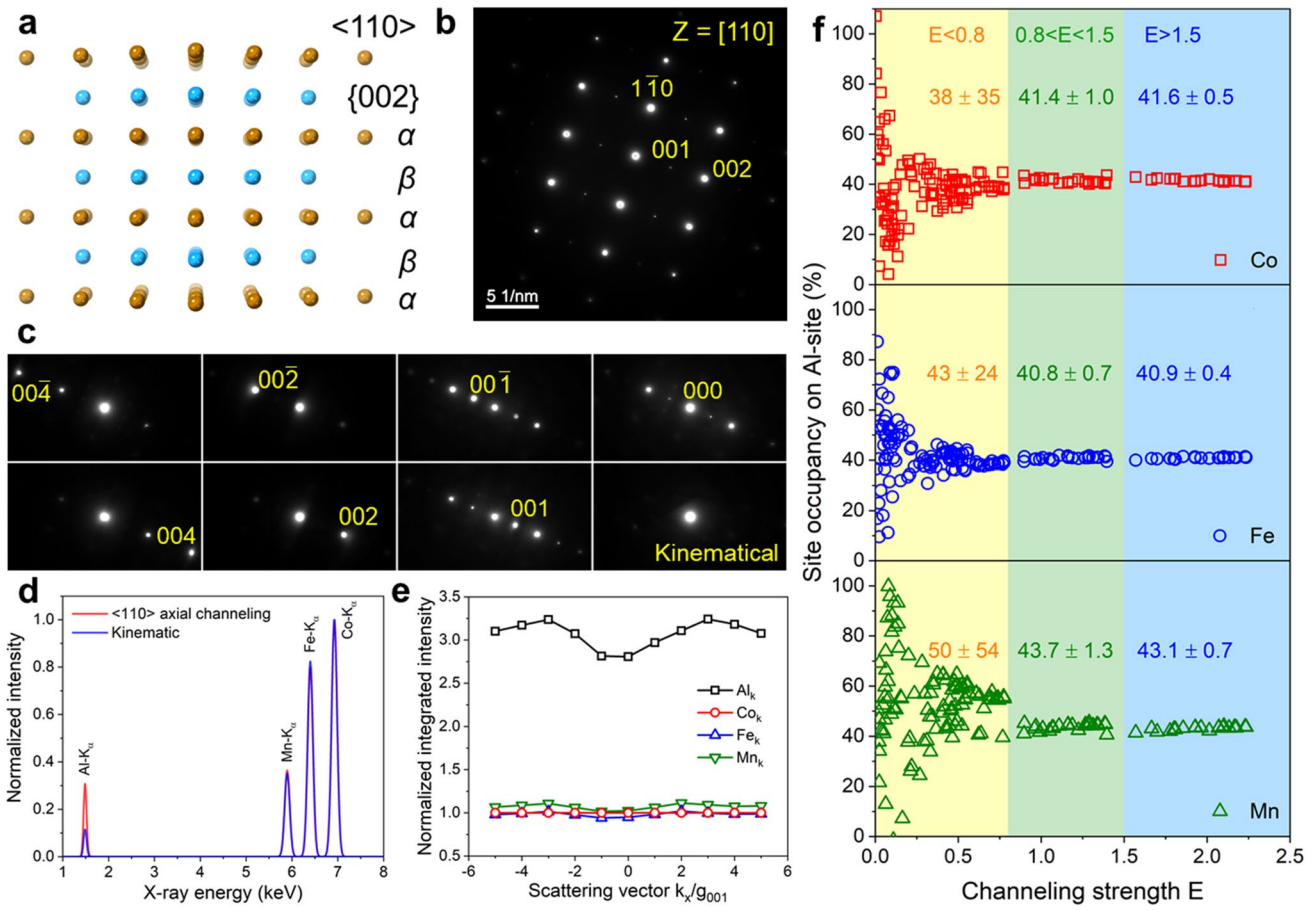

Fig. 4 ALCHEMI analysis for B2-ordered $Fe_{30}Co_{40}Mn_{15}Al_{15}$. **a** Projection of atoms along channeling <110> zone axis orientation showing sublattice α-site and β-site for a B2 phase. SAED patterns showing beam incidence directions **b** along a <110> zone axis and **c** tilted along (002) Kikuchi band near a <110> zone axis. **d** EDS spectra (normalized by Co-K_α) collected along <110> zone axis and in a kinematical scattering condition. **e** Normalized integrated X-ray intensity plotted against scattering vectors k_x/g_{001} near <110> direction; the intensities were first normalized to that of the Co-K_α peak and then normalized by their respective kinematical/non-channeling counterparts. **f** Site occupation fraction of Co, Fe, and Mn elements on Al-site as a function of channeling strength E (defined in Note S2)

We also made efforts to further quantify the site occupancy of the alloying elements in the B2 lattice (see detailed calculations in Note S2). The quantitative site occupancy results for Co, Fe, and Mn elements on Al-site as a function of channeling strength E (defined in Equation S7 in Note S2) are summarized in Fig. 4f, where the channeling strength E classifies the accuracy of the site occupancy quantification. Generally, higher channeling strength values provide better accuracy as the channeling effect is stronger [38, 39]. It is noted that the Al data points are not displayed since the Al atoms preferentially occupy one site (Al-site). It is readily seen that the data points of site occupancy percentage on the Al-site for Co, Fe, and Mn can be divided into three regimes and the site occupancy values significantly converge with small standard deviations for stronger channeling regimes ($0.8 < E < 1.5$ and $E > 1.5$), Specifically, $41.6 \pm 0.5\%$ Co, $40.9 \pm 0.4\%$ Fe, and $43.1 \pm 0.7\%$ Mn are determined to occupy the Al-site based on the strongest channeling regime ($E > 1.5$), and the rest resides on the other site (Al-anti-site) of the B2 lattice.

Magnetic Behavior

The magnetic hysteresis loops of both the as-cast material and specimens annealed for 75 h at 873 K, 1073 K and 1273 K are shown in Fig. 5a and the corresponding saturation magnetization (M_s) and coercivity (H_c) are summarized in Fig. 5c and listed in Table S1. It is noted that demagnetizing field corrections are performed for the hysteresis loops in the study (see details in Note S3). The as-cast MPEA exhibits good combination of high M_s of 162.4 ± 1.0 Am^2 kg^{-1} and low H_c of 113.6 ± 16.5 A m^{-1}, indicating its potential as a soft magnetic material. After annealing at 873 K for 75 h, the MPEA maintains the soft magnetic properties, i.e., a high M_s of 163.4 ± 0.4 Am^2 kg^{-1} and a low coercivity of 127.0 ± 16.1 A m^{-1}. However, higher temperature

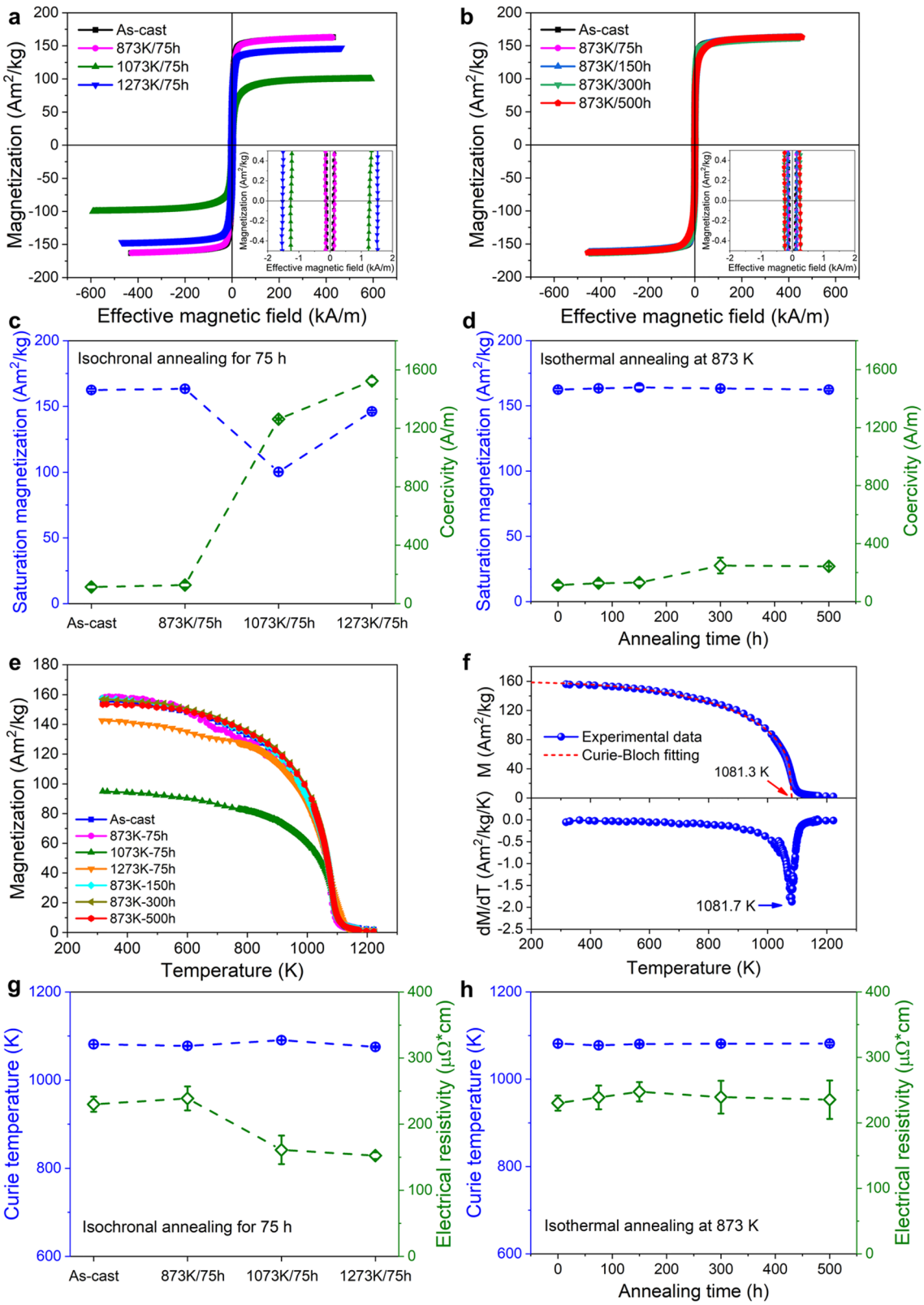

heat treatments significantly degrade the soft magnetic properties of the MPEA to $M_s = 100.2 \pm 0.2$ Am^2 kg^{-1} and $H_c = 1262.8 \pm 6.8$ A m^{-1} at 1073 K, and to $M_s = 146.2 \pm 0.9$ Am^2 kg^{-1} and $H_c = 1524.5 \pm 26.0$ A m^{-1} at 1273 K, as shown in Fig. 5a and c and Table S1. These high values of H_c are even beyond the scope of soft magnetic materials ($H_c < 1000$

◂**Fig. 5** Soft magnetic behavior of $Fe_{30}Co_{40}Mn_{15}Al_{15}$. **a** Representative magnetic hysteresis loops and **c** the corresponding summarized plot of saturation magnetization and coercivity of as-cast, 873 K–75 h, 1073 K–75 h, and 1273 K–75 h specimens. **b** Hysteresis loops and **d** the corresponding summarized plot of saturation magnetization and coercivity of specimens heat-treated at 873 K for 75 h, 150 h, 300 h and 500 h, respectively. The insets in (**a**, **b**) are enlarged view of the loops at low magnetic fields. **e** Temperature-dependent magnetization for as-cast and various heat-treated samples at an applied magnetic field of 400 kA m^{-1}. **f** Representative temperature-dependent magnetization of as-cast specimen depicted by Curie–Bloch equation (upper) and the derivative of the magnetization (d*M*/d*T*) versus temperature curve (lower). Summarized plots of curie temperature (left axes) and electrical resistivity (right axes) of **g** isochronal annealing for 75 h and **h** isothermal annealing at 873 K

A m^{-1} for soft magnetic materials). The deterioration of soft magnetic properties is presumably caused by the high-density FCC phase (Figs. 1, 2).

In order to further demonstrate the thermal stability of the soft magnetic properties, hysteresis loops for specimens annealed at 873 K for prolonged durations of 150 h, 300 h and 500 h are presented in Fig. 5b, and the soft magnetic properties are summarized in Fig. 5d and Table S1. It is readily seen that hysteresis loops almost overlap with each other for all anneals at 873 K. Specifically, the M_s still preserves the high value of 162.4 ± 0.9 Am^2 kg^{-1} for anneals up to 500 h. Although the H_c gradually increases with the heat-treatment time to 243.2 ± 1.4 A m^{-1} for 500 h duration, it is still relatively good as a soft magnetic material. This slight increment of H_c is probably associated with the small fraction of FCC precipitates (Fig. 3).

Figure 5e presents the temperature dependence of the magnetizations of the MPEA upon heating from 323 to 1223 K in an applied magnetic field of 400 kA m^{-1}. Although the 1073 K (green curve) and 1273 K (orange curve) heat-treated samples exhibit lower magnetizations, the temperature-dependent trends are essentially similar for all specimens, namely, the magnetizations initially decrease gradually with the increase in temperature from room temperature to ~ 1000 K, followed by a dramatic drop, reaching values close to zero at $T > 1100$ K, indicative of similar Curie temperatures. The temperature-dependent magnetization for ferromagnetic materials can be described by the Curie–Bloch equation $M(T) = M(0)\left[1 - \left(T/T_c\right)^{\alpha}\right]^{\beta}$ [50], where $M(0)$ is the magnetization at 0 K, T_c is the Curie temperature at which the magnetization vanishes, α is the Bloch exponent, and $\beta \approx 1/3$ is the critical magnetization exponent. The upper Fig. 5f represents a fitting result for as-cast specimen, which gives a high Curie temperature of 1081.3 K. Alternatively, the Curie temperature can be determined to be 1081.7 K (lower Fig. 5f) via the minimum of the derivative of the magnetization (d*M*/d*T*) versus temperature curve, corresponding to the steepest slope point, which agrees well with the Curie–Bloch fitting results. All Curie temperatures were obtained by averaging the values mentioned above and they are summarized in Fig. 5g and h and Table S1, which preserves the high Curie temperatures (1075–1090 K) for all anneals with few variations. The combination of high thermal stability with good soft magnetic properties at 873 K up to 500 h (Fig. 5b, d) and high Curie temperature suggests that the MPEA has the potential for high-temperature soft magnetic applications.

The variation of electrical resistivity (ρ) for as-cast and annealed samples are also plotted in Fig. 5g and h and tabulated in Table S1. The as-cast alloy has a high resistivity of ~ 230 μΩ cm, suggesting a low eddy current loss, while 1073 K and 1273 K anneals tend to decrease the resistivities (or increase the conductivities). This could be associated with the precipitation of the FCC phase (Figs. 1, 2), resulting in a reduction of the scattering of conducting electrons due to dissolved solute atoms, which is commonly observed in other alloys [51]. However, the high electrical resistivities are retained for all 873 K anneals for up to 500 h, further implying its high-temperature potential. Further comparisons with other reported conventional and MPEA soft magnetic materials regarding the soft magnetic properties and electrical resistivity will be discussed.

First-Principles Calculations

Density functional theory (DFT) calculations were performed to understand the magnetic behavior of $Fe_{30}Co_{40}Mn_{15}Al_{15}$. In the calculations, the initial magnetic moments of Fe, Co, and Al atoms were set to be parallel with each other according to their common magnetic forms in metals and binary alloys. Elemental Mn is antiferromagnetic; however, the magnetic states of Mn in alloy systems can be complicated [21, 52]. We explored four initial states of the Mn moment, namely, Mn moments parallel to the other atoms; Mn moments anti-parallel to the other atoms; Mn moments on Al-sites parallel while those on Al-anti-sites anti-parallel; and Mn moments on Al-sites anti-parallel while those on Al-anti-sites parallel. The initial state of parallel Mn spins, i.e., the ferromagnetic state, yielded the lowest energy (~ 0.02 eV $atom^{-1}$ lower than the other three) in all the three SQSs, and therefore the corresponding results were adopted to represent the alloy's magnetic properties. Figure 6a–e show the total density of states (DOS) of a SQS and the corresponding partial DOS (pDOS) for each element, respectively. The pDOS of Co, Fe, Mn atoms exhibit a significantly higher spin up than spin down distribution, a typical ferromagnetic behavior, while the pDOS of Al is non-magnetic (note the small *y*-axis scale of pDOS of Al element). As a result, the total DOS exhibits a more pronounced spin up than spin down distribution (Fig. 6a). We also calculated the

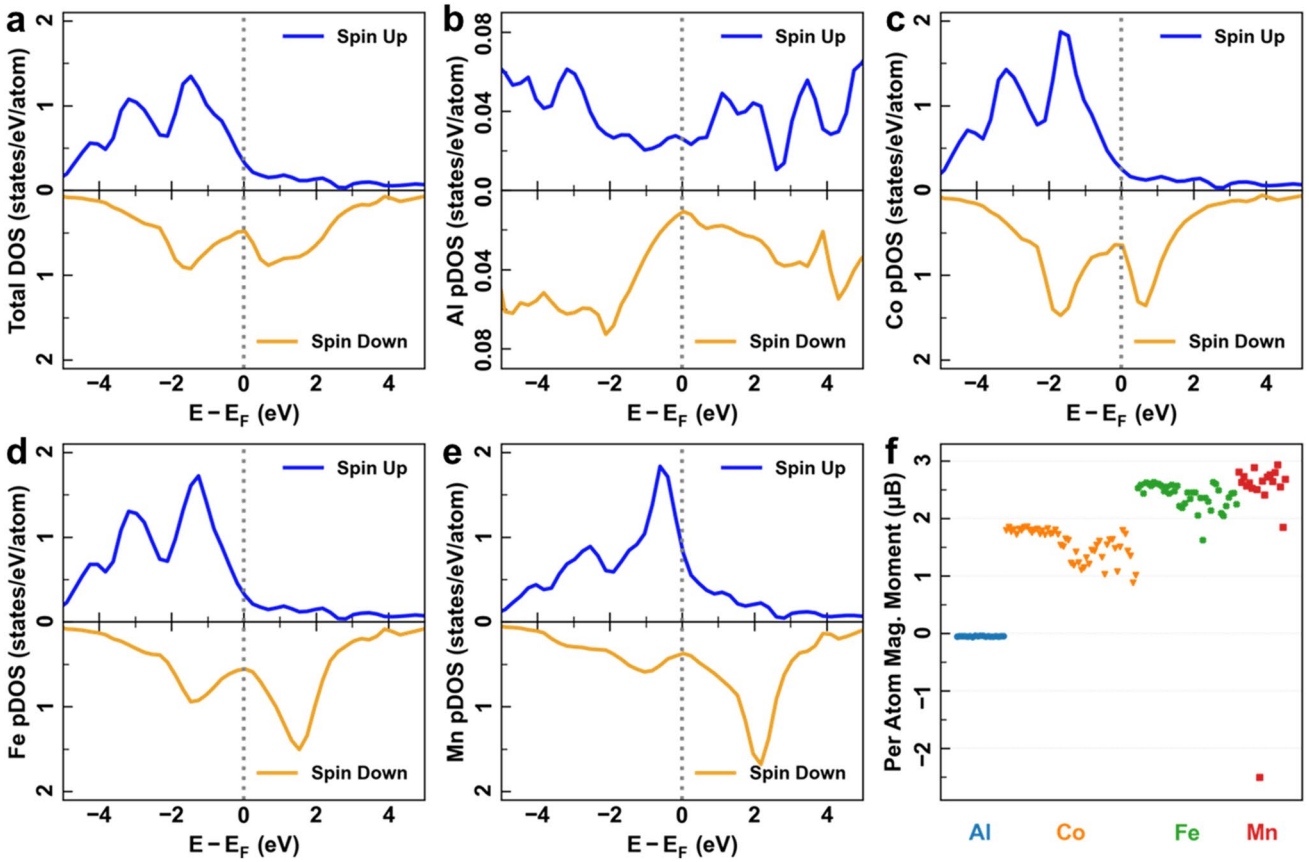

Fig. 6 DFT calculations. **a** Total DOS, **b**–**e** pDOS of Al, Co, Fe, and Mn atoms, **f** calculated elemental magnetic moments for $Fe_{30}Co_{40}Mn_{15}Al_{15}$

atomic magnetic moments of all elements, as shown in Fig. 6f. The magnetic moments of Al atoms essentially display a near zero moment, while the average per atom magnetic moments for Co, Fe, and Mn are 1.56, 2.40, and 2.35 μ_B, respectively, where μ_B is Bohr magneton. All Co and Fe atoms exhibit parallel spin arrangements, as do most of the Mn atoms. The favored ferromagnetic state of Mn is due to the presence of the Al atoms, as it was suggested that the Al can significantly reduce the Mn *d*-orbital width and increase its exchange splitting, shifting the antiferromagnetic order of Mn to ferromagnetic order [21, 52]. The saturation magnetization is correlated with magnetic moments via the expression $M_s = \mu_{B,\ supercell}/W_{supercell}$, where the M_s is in units of $Am^2\ kg^{-1}$, $\mu_{B,\ supercell}$ is the total magnetic moments in the supercell ($\mu_B = 9.274 \times 10^{-24}\ Am^2$), and $W_{supercell}$ is the total atomic weight of the supercell. As a result, the DFT calculations predict an averaged theoretical saturation magnetization of 179.4 $Am^2\ kg^{-1}$, which is well close to the experimentally determined value of 162.4 $Am^2\ kg^{-1}$ measured using the VSM, considering that the DFT calculations were performed at 0 K whereas the VSM measurements were conducted at room temperature.

Comparison of Soft Magnetic Properties

To provide insight into the soft magnetic properties, the M_s and H_c of $Fe_{30}Co_{40}Mn_{15}Al_{15}$ and a variety of MPEAs reported in the literature [18–27, 52–64] are summarized in Fig. 7a and in Table S2. It is clearly seen that the data pair for $Fe_{30}Co_{40}Mn_{15}Al_{15}$, located in the upper left corner, displays quite appealing soft magnetic properties with the lowest H_c yet highest M_s in comparison with other reported MPEAs so far. It is particularly noted that most research on MPEAs is mainly focused on simple solid-solution alloys or alloys with precipitates, e.g., either BCC or FCC, or a mixture of disordered and/or ordered phases (a mixture of two or three of FCC, BCC, $L1_2$, B2 or $L2_1$ as listed in Table S2).

The soft magnet stoichiometric FeCo and the commercial alloy FeCo–2V [25, 53–57] are also included for further comparison. Although $Fe_{30}Co_{40}Mn_{15}Al_{15}$ has a lower M_s than stoichiometric FeCo, it exhibits a much lower H_c. The binary B2 FeCo alloys are extremely brittle [65], and

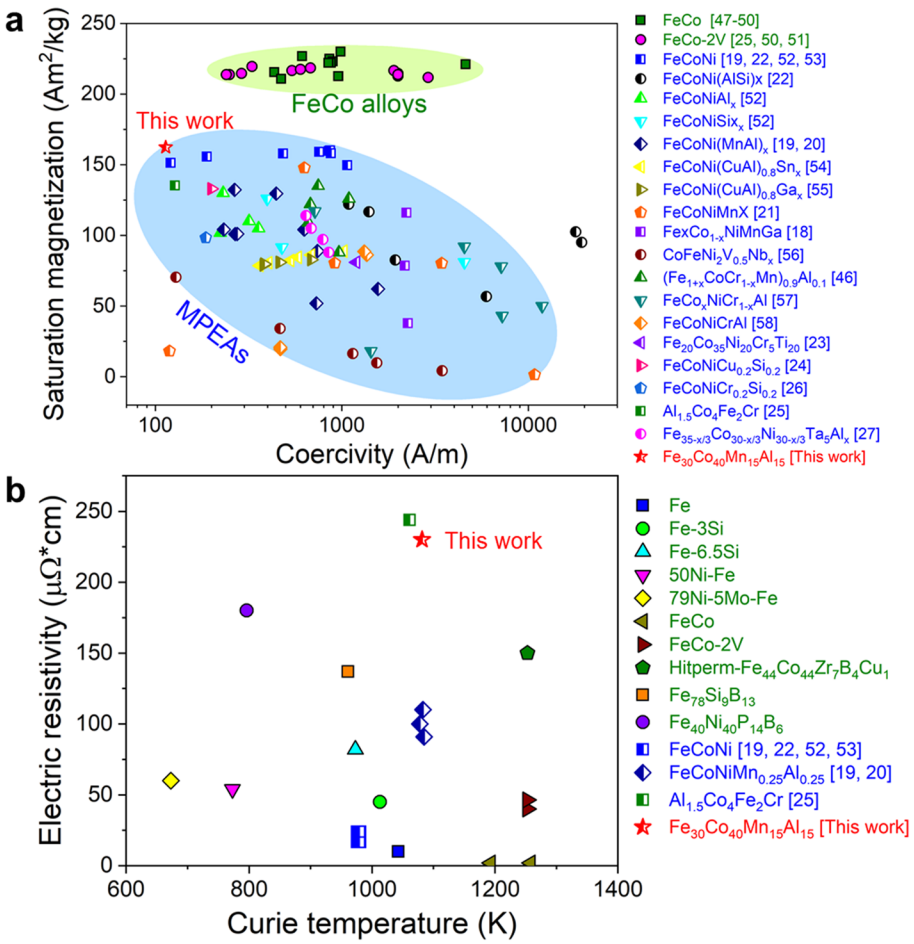

Fig. 7 Soft magnetic properties and electric resistivity of $Fe_{30}Co_{40}Mn_{15}Al_{15}$ in comparison with traditional and previously reported MPEAs soft magnets. **a** Comparisons of saturation magnetization and coercivity of $Fe_{30}Co_{40}Mn_{15}Al_{15}$ with other reported MPEAs and conventional FeCo alloys in the literature [18–27, 52–64]. **b** Comparisons of electrical resistivity and Curie temperature of $Fe_{30}Co_{40}Mn_{15}Al_{15}$ with other soft magnetic materials (adapted from Ref. [25]). Solid and half-solid symbols represent traditional and MEPAs soft magnetic materials, respectively

thus ~ 2 wt% V was added for the commercial FeCo–2V soft magnetic alloys to moderately improve the ductility and workability of FeCo yet negligibly compromises the soft magnetic properties [65]. However, precipitation of $L1_2$-structured $(FeCo)_3V$ can occur in FeCo–2V at relatively low temperatures, e.g., 773 K, which significantly degrades the soft magnetic properties for high-temperature applications [32, 66]. In contrast, $Fe_{30}Co_{40}Mn_{15}Al_{15}$ exhibits good thermal stability, i.e., phase separation does not occur until above 873 K (Fig. 1). Further, $Fe_{30}Co_{40}Mn_{15}Al_{15}$ also enables a reduction in the cost in comparison with the FeCo–2V commercial alloys due to the decreased content or replacement of the high-cost elements Co and V via substantially alloying with the inexpensive Mn and Al. It is also worth noting that the soft magnetic properties of the MPEA can be further optimized through tuning the microstructures, e.g., producing nanocrystalline soft magnets, and compositions, e.g., via alloying minor element additions.

For soft magnetic materials, high electrical resistivity (ρ) is usually desired since higher ρ leads to lower eddy current loss [67], especially at high temperatures. Meanwhile, a high Curie temperature (T_c) is also considered important to make the material a potential candidate for high-temperature soft magnetic applications. Thus, the electrical resistivity and Curie temperature of $Fe_{30}Co_{40}Mn_{15}Al_{15}$ and some soft magnetic materials are compiled and compared, as shown in Fig. 7b and Table S2. Those data points for traditional soft magnets in Fig. 7b are adapted from Ref. [25] and thus are not included in Table S2 for brevity. It is readily seen that $Fe_{30}Co_{40}Mn_{15}Al_{15}$ exhibits a good combination of high electrical resistivity (230 μΩ cm) and Curie temperature (1081 K), located in the upper right corner, which is better than most of the typical soft magnetic materials, e.g., electrical steels, FeCo–2V alloys, amorphous alloys, nanocrystalline alloys, and HEAs/MEAs. For instance, the equiatomic FeCoNi MEA and aforementioned commercial FeCo–2V alloys exhibit low electrical resistivity and, thus, suffer high eddy current losses. The recently developed $Al_{1.5}Co_4Fe_2Cr$ HEA [25] shows the most comparable combination of ρ and T_c to $Fe_{30}Co_{40}Mn_{15}Al_{15}$, but higher M_s and slightly lower H_c are obtained for $Fe_{30}Co_{40}Mn_{15}Al_{15}$. In summary, $Fe_{30}Co_{40}Mn_{15}Al_{15}$ exhibits a good combination of low H_c, high M_s, high T_c, high ρ, and high thermal stability, which makes it a potential candidate for high-temperature soft magnetic applications.

Conclusions

In this study, a novel soft magnetic single-phase B2-ordered $Fe_{30}Co_{40}Mn_{15}Al_{15}$ MPEA was developed. The as-cast B2 MPEA shows good chemical homogeneity as confirmed via combined characterizations using synchrotron XRD, SEM/BSE, TEM, and APT. TEM-based ALCHEMI analysis indicates that the Al atoms preferentially occupy one sublattice site whereas the other elements tend to partition between both sublattice sites in the B2 lattice. Good soft magnetic properties with high saturation magnetization of ~ 162.4 $Am^2\ kg^{-1}$, high Curie temperature of ~ 1081 K, low coercivity of 113.6 A m^{-1}, and high electrical resistivity of 230 μΩ cm were obtained for the as-cast alloy, which outperforms other MPEAs reported in the literature. The good soft magnetic properties are well retained after long-term annealing at 873 K for up to 500 h ($M_s = 162.4\ Am^2\ kg^{-1}$ and $H_c = 243.2$ A m^{-1}) due to the good thermal stability of the B2 phase. DFT calculations predict magnetic properties consistent with the experimental results and indicate that Fe, Co, and Mn elements predominately contribute to the ferromagnetism. The good magnetic properties and good thermal stability up to 873 K suggest that the MPEA has potential for use with wide-bandgap semiconductors that operate at high temperatures.

Supplementary Information The online version contains supplementary material available at https://doi.org/10.1007/s44210-022-00005-5.

Acknowledgements This work was supported by NIST Grant 60NANB2D0120 and U.S. National Science Foundation Grant Number 1758924. L.X. and H.X. are supported by the National Science Foundation under Grant No. DMR-1654438. This work used the Extreme Science and Engineering Discovery Environment (XSEDE), which is supported by the National Science Foundation Grant Number TG-DMR17012. This research used resources of the Advanced Photon Source, a U.S. Department of Energy (DOE) Office of Science User Facility, operated for the DOE Office of Science by Argonne National Laboratory under Contract No. DE-AC02-06CH11357. We would like to thank Dr. Qi Zeng at Materion Corporation for technical discussion and suggestions on magnetic behavior. The views and conclusions contained herein are those of the authors and should not be interpreted as necessarily representing official policies, either expressed or implied, of the National Science Foundation, or the U.S. Government.

Declarations

Conflict of interest The authors declare no conflict of interest.

References

1. J.M. Silveyra, E. Ferrara, D.L. Huber, T.C. Monson, Soft magnetic materials for a sustainable and electrified world. Science **362**(6413), eaao0195 (2018)
2. V. Chaudhary, R. Chaudhary, R. Banerjee, R.V. Ramanujan, Accelerated and conventional development of magnetic high entropy alloys. Mater. Today **49**, 231–252 (2021)
3. J.W. Yeh, S.K. Chen, S.J. Lin, J.Y. Gan, T.S. Chin, T.T. Shun, C.H. Tsau, S.Y. Chang, Nanostructured high-entropy alloys with multiple principal elements: novel alloy design concepts and outcomes. Adv. Eng. Mater. **6**(5), 299–303 (2004)
4. B. Cantor, I.T.H. Chang, P. Knight, A.J.B. Vincent, Microstructural development in equiatomic multicomponent alloys. Mater. Sci. Eng. A **375**, 213–218 (2004)
5. D.B. Miracle, O.N. Senkov, A critical review of high entropy alloys and related concepts. Acta Mater. **122**, 448–511 (2017)
6. R. Zhang, S. Zhao, J. Ding, Y. Chong, T. Jia, C. Ophus, M. Asta, R.O. Ritchie, A.M. Minor, Short-range order and its impact on the CrCoNi medium-entropy alloy. Nature **581**(7808), 283–287 (2020)
7. B. Gludovatz, A. Hohenwarter, D. Catoor, E.H. Chang, E.P. George, R.O. Ritchie, A fracture-resistant high-entropy alloy for cryogenic applications. Science **345**(6201), 1153–1158 (2014)
8. Y.X. Ye, B. Ouyang, C.Z. Liu, G.J. Duscher, T.G. Nieh, Effect of interstitial oxygen and nitrogen on incipient plasticity of NbTiZrHf high-entropy alloys. Acta Mater. **199**, 413–424 (2020)
9. Q. Ding, Y. Zhang, X. Chen, X. Fu, D. Chen, S. Chen, L. Gu, F. Wei, H. Bei, Y. Gao, Tuning element distribution, structure and properties by composition in high-entropy alloys. Nature **574**(7777), 223–227 (2019)
10. Y. Yang, T. Chen, L. Tan, J.D. Poplawsky, K. An, Y. Wang, G.D. Samolyuk, K. Littrell, A.R. Lupini, A. Borisevich, E.P. George, Bifunctional nanoprecipitates strengthen and ductilize a medium-entropy alloy. Nature **595**(7866), 245–249 (2021)
11. Z. Lei, X. Liu, Y. Wu, H. Wang, S. Jiang, S. Wang, X. Hui, Y. Wu, B. Gault, P. Kontis, D. Raabe, L. Gu, Q. Zhang, H. Chen, H. Wang, J. Liu, K. An, Q. Zeng, T.-G. Nieh, Z. Lu, Enhanced strength and ductility in a high-entropy alloy via ordered oxygen complexes. Nature **563**, 546–550 (2018)
12. Z. Wang, I. Baker, Z. Cai, S. Chen, J.D. Poplawsky, W. Guo, The effect of interstitial carbon on the mechanical properties and dislocation substructure evolution in $Fe_{40.4}Ni_{11.3}Mn_{34.8}Al_{7.5}Cr_6$ high entropy alloys. Acta Mater. **120**, 228–239 (2016)
13. R. Feng, Y. Rao, C. Liu, X. Xie, D. Yu, Y. Chen, M. Ghazisaeidi, T. Ungar, H. Wang, K. An, P.K. Liaw, Enhancing fatigue life by ductile-transformable multicomponent B2 precipitates in a high-entropy alloy. Nat. Commun. **12**(1), 1–10 (2021)
14. Y.Y. Zhao, H.W. Chen, Z.P. Lu, T.G. Nieh, Thermal stability and coarsening of coherent particles in a precipitation-hardened $(NiCoFeCr)_{94}Ti_2Al_4$ high-entropy alloy. Acta Mater. **147**, 184–194 (2018)
15. H. Jiang, D. Qiao, Y. Lu, Z. Ren, Z. Cao, T. Wang, T. Li, Direct solidification of bulk ultrafine-microstructure eutectic high-entropy alloys with outstanding thermal stability. Scr. Mater. **165**, 145–149 (2019)
16. Y.X. Ye, C.Z. Liu, H. Wang, T.G. Nieh, Friction and wear behavior of a single-phase equiatomic TiZrHfNb high-entropy alloy studied using a nanoscratch technique. Acta Mater. **147**, 78–89 (2018)
17. Y.Y. Zhao, Y.X. Ye, C.Z. Liu, R. Feng, K.F. Yao, T.G. Nieh, Tribological behavior of an amorphous $Zr_{20}Ti_{20}Cu_{20}Ni_{20}Be_{20}$ high-entropy alloy studied using a nanoscratch technique. Intermetallics **113**, 106561 (2019)
18. T. Zuo, M. Zhang, P.K. Liaw, Y. Zhang, Novel high entropy alloys of $Fe_xCo_{1-x}NiMnGa$ with excellent soft magnetic properties. Intermetallics **100**, 1–8 (2018)
19. P. Li, A. Wang, C.T. Liu, Composition dependence of structure, physical and mechanical properties of $FeCoNi(MnAl)_x$ high entropy alloys. Intermetallics **87**, 21–26 (2017)

20. P. Li, A. Wang, C.T. Liu, A ductile high entropy alloy with attractive magnetic properties. J. Alloys Compd. **694**, 55–60 (2017)
21. T. Zuo, M.C. Gao, L. Ouyang, X. Yang, Y. Cheng, R. Feng, S. Chen, P.K. Liaw, J.A. Hawk, Y. Zhang, Tailoring magnetic behavior of CoFeMnNiX (X = Al, Cr, Ga, and Sn) high entropy alloys by metal doping. Acta Mater. **130**, 10–18 (2017)
22. Y. Zhang, T. Zuo, Y. Cheng, P.K. Liaw, High-entropy alloys with high saturation magnetization, electrical resistivity, and malleability. Sci. Rep. **3**, 1455 (2013)
23. R.K. Mishra, R.R. Shahi, Novel $Co_{35}Cr_5Fe_{20}Ni_{20}Ti_{20}$ high entropy alloy for high magnetization and low coercivity. J. Magn. Magn. Mater. **484**, 83–87 (2019)
24. C. Chen, H. Zhang, Y. Fan, W. Zhang, R. Wei, T. Wang, T. Zhang, F. Li, A novel ultrafine-grained high entropy alloy with excellent combination of mechanical and soft magnetic properties. J. Magn. Magn. Mater. **502**, 166513 (2020)
25. Y. Ma, Q. Wang, X. Zhou, J. Hao, B. Gault, Q. Zhang, C. Dong, T.-G. Nieh, A novel soft-magnetic B2-based multiprincipal-element alloy with a uniform distribution of coherent body-centered-cubic nanoprecipitates. Adv. Mater. **33**(14), 2006723 (2021)
26. H. Zhang, Y. Yang, L. Liu, C. Chen, T. Wang, R. Wei, T. Zhang, Y. Dong, F. Li, A novel $FeCoNiCr_{0.2}Si_{0.2}$ high entropy alloy with an excellent balance of mechanical and soft magnetic properties. J. Magn. Magn. Mater. **478**, 116–121 (2019)
27. L. Han, Z. Rao, I.R. Souza Filho, F. Maccari, Y. Wei, G. Wu, A. Ahmadian, X. Zhou, O. Gutfleisch, D. Ponge, D. Raabe, Z. Li, Ultrastrong and ductile soft magnetic high-entropy alloys via coherent ordered nanoprecipitates. Adv. Mater. **33**, 2102139 (2021)
28. J. Xu, J.Y. Zhang, Y.Q. Wang, P. Zhang, J. Kuang, G. Liu, G.J. Zhang, J. Sun, Annealing-dependent microstructure, magnetic and mechanical properties of high-entropy $FeCoNiAl_{0.5}$ alloy. Mater. Sci. Eng. A **776**, 139003 (2020)
29. Z. Fu, B.E. MacDonald, A.D. Dupuy, X. Wang, T.C. Monson, R.E. Delaney, C.J. Pearce, K. Hu, Z. Jiang, Y. Zhou, Exceptional combination of soft magnetic and mechanical properties in a heterostructured high-entropy composite. Appl. Mater. Today **15**, 590–598 (2019)
30. S. Dasari, V. Chaudhary, B. Gwalani, A. Jagetia, V. Soni, S. Gorsse, R.V. Ramanujan, R. Banerjee, Highly tunable magnetic and mechanical properties in an $Al_{0.3}$CoFeNi complex concentrated alloy. Materialia **12**, 100755 (2020)
31. Z. Rao, B. Dutta, F. Körmann, W. Lu, X. Zhou, C. Liu, A.K. da Silva, U. Wiedwald, M. Spasova, M. Farle, Beyond solid solution high-entropy alloys: tailoring magnetic properties via spinodal decomposition. Adv. Funct. Mater. **31**(7), 2007668 (2021)
32. R.H. Yu, S. Basu, L. Ren, Y. Zhang, A. Parvizi-Majidi, K.M. Unruh, J.Q. Xiao, High temperature soft magnetic materials: FeCo alloys and composites. IEEE Trans. Magn. **36**(5), 3388–3393 (2000)
33. R.H. Yu, S. Basu, Y. Zhang, J.Q. Xiao, Magnetic domains and coercivity in FeCo soft magnetic alloys. J. Appl. Phys. **85**(8), 6034–6036 (1999)
34. P. Gupta, P. Švec, A.K. Sinha, S.R. Kane, A. Pandey, S.K. Rai, T. Ganguli, Correlation of B2 super-lattice ordering with soft magnetic and mechanical properties of nanocrystalline FeCoNbB HITPERM alloys. Mater. Res. Express **6**(2), 026537 (2018)
35. M.S.K.K.Y. Nartu, S. Dasari, A. Sharma, V. Chaudhary, S.M. Varahabhatla, S.A. Mantri, E. Ivanov, R.V. Ramanujan, N.B. Dahotre, R. Banerjee, Reducing coercivity by chemical ordering in additively manufactured soft magnetic Fe–Co (Hiperco) alloys. J. Alloys Compd. **861**, 157998 (2021)
36. P. Munroe, I. Baker, Effect of accelerating voltage on planar and axial channeling in ordered intermetallic compounds. J. Mater. Res. **7**(8), 2119–2125 (1992)
37. Z. Horita, S. Matsumura, T. Baba, General formulation for ALCHEMI. Ultramicroscopy **58**(3–4), 327–335 (1995)
38. C.H. Liebscher, J. Preussner, R. Voelkl, U. Glatzel, Atomic site location by channelling enhanced microanalysis (ALCHEMI) in γ′-strengthened Ni- and Pt-base alloys. Acta Mater. **56**(16), 4267–4276 (2008)
39. L. Wang, M. Oehring, Y. Liu, U. Lorenz, F. Pyczak, Site occupancy of alloying elements in the $L1_2$ structure determined by channeling enhanced microanalysis in γ/γ′ Co-9Al-9W-2X alloys. Acta Mater. **162**, 176–188 (2019)
40. G. Kresse, J. Furthmüller, Efficiency of ab-initio total energy calculations for metals and semiconductors using a plane-wave basis set. Comput. Mater. Sci. **6**(1), 15–50 (1996)
41. G. Kresse, J. Hafner, Ab initio molecular dynamics for liquid metals. Phys. Rev. B **47**(1), 558 (1993)
42. J.P. Perdew, K. Burke, M. Ernzerhof, Generalized gradient approximation made simple. Phys. Rev. Lett. **77**(18), 3865 (1996)
43. P.E. Blöchl, Projector augmented-wave method. Phys. Rev. B **50**(24), 17953 (1994)
44. A. Zunger, S.-H. Wei, L.G. Ferreira, J.E. Bernard, Special quasirandom structures. Phys. Rev. Lett. **65**, 353–356 (1990)
45. A. Van de Walle, P. Tiwary, M. De Jong, D. Olmsted, M. Asta, A. Dick, D. Shin, Y. Wang, L.-Q. Chen, Z.-K. Liu, Efficient stochastic generation of special quasirandom structures. Calphad **42**, 13–18 (2013)
46. A. Van De Walle, M. Asta, G. Ceder, The alloy theoretic automated toolkit: a user guide. Calphad **26**(4), 539–553 (2002)
47. B. Gault, M.P. Moody, J.M. Cairney, S.P. Ringer, *Atom Probe Microscopy* (Springer Science & Business Media, New York, 2012)
48. X. Yang, Y. Zhang, Prediction of high-entropy stabilized solid-solution in multi-component alloys. Mater. Chem. Phys. **132**(2–3), 233–238 (2012)
49. S. Guo, Q. Hu, C. Ng, C.T. Liu, More than entropy in high-entropy alloys: forming solid solutions or amorphous phase. Intermetallics **41**, 96–103 (2013)
50. R.F.L. Evans, U. Atxitia, R.W. Chantrell, Quantitative simulation of temperature-dependent magnetization dynamics and equilibrium properties of elemental ferromagnets. Phys. Rev. B **91**(14), 144425 (2015)
51. Y. Ye, X. Yang, J. Wang, X. Zhang, Z. Zhang, T. Sakai, Enhanced strength and electrical conductivity of Cu–Zr–B alloy by double deformation–aging process. J. Alloys Compd. **615**, 249–254 (2014)
52. C. Jung, K. Kang, A. Marshal, K.G. Pradeep, J.-B. Seol, H.M. Lee, P.-P. Choi, Effects of phase composition and elemental partitioning on soft magnetic properties of AlFeCoCrMn high entropy alloys. Acta Mater. **171**, 31–39 (2019)
53. Q. Zeng, I. Baker, V. McCreary, Z. Yan, Soft ferromagnetism in nanostructured mechanical alloying FeCo-based powders. J. Magn. Magn. Mater. **318**(1–2), 28–38 (2007)
54. A.J. Albaaji, E.G. Castle, M.J. Reece, J.P. Hall, S.L. Evans, Enhancement in the elongation, yield strength and magnetic properties of intermetallic FeCo alloy using spark plasma sintering. J. Mater. Sci. **52**(22), 13284–13295 (2017)
55. A.J. Albaaji, E.G. Castle, M.J. Reece, J.P. Hall, S.L. Evans, Influence of spark plasma sintering parameters on magnetic properties of FeCo alloy. AIP Adv. **8**(4), 047705 (2018)
56. A.I.C. Persiano, R.D. Rawlings, Effect of niobium additions on the structure and magnetic properties of equiatomic iron–cobalt alloys. J. Mater. Sci. **26**(15), 4026–4032 (1991)
57. K. Kawahara, M. Uehara, A possibility for developing high strength soft magnetic materials in FeCo-X alloys. J. Mater. Sci. **19**(8), 2575–2581 (1984)

58. T.T. Zuo, R.B. Li, X.J. Ren, Y. Zhang, Effects of Al and Si addition on the structure and properties of CoFeNi equal atomic ratio alloy. J. Magn. Magn. Mater. **371**, 60–68 (2014)
59. M.S.K.K.Y. Nartu, A. Jagetia, V. Chaudhary, S.A. Mantri, E. Ivanov, N.B. Dahotre, R.V. Ramanujan, R. Banerjee, Magnetic and mechanical properties of an additively manufactured equiatomic CoFeNi complex concentrated alloy. Scr. Mater. **187**, 30–36 (2020)
60. Z. Li, C. Wang, L. Yu, Y. Gu, M. Pan, X. Tan, H. Xu, Magnetic properties and microstructure of $FeCoNi(CuAl)_{0.8}Sn_x$ ($0 \le x \le 0.10$) high-entropy alloys. Entropy **20**(11), 872 (2018)
61. Z. Li, H. Xu, Y. Gu, M. Pan, L. Yu, X. Tan, X. Hou, Correlation between the magnetic properties and phase constitution of $FeCoNi(CuAl)_{0.8}Ga_x$ ($0 \le x \le 0.08$) high-entropy alloys. J. Alloys Compd. **746**, 285–291 (2018)
62. L. Jiang, Y. Lu, Y. Dong, T. Wang, Z. Cao, T. Li, Effects of Nb addition on structural evolution and properties of the $CoFeNi_2V_{0.5}$ high-entropy alloy. Appl. Phys. A **119**(1), 291–297 (2015)
63. T. Borkar, V. Chaudhary, B. Gwalani, D. Choudhuri, C.V. Mikler, V. Soni, T. Alam, R.V. Ramanujan, R. Banerjee, A combinatorial approach for assessing the magnetic properties of high entropy alloys: role of Cr in $AlCo_xCr_{1-x}FeNi$. Adv. Eng. Mater. **19**(8), 1700048 (2017)
64. C. Zhao, J. Li, Y. He, J. Wang, W.Y. Wang, H. Kou, J. Wang, Effect of strong magnetic field on the microstructure and mechanical-magnetic properties of AlCoCrFeNi high-entropy alloy. J. Alloys Compd. **820**, 153407 (2020)
65. E.P. George, A.N. Gubbi, I. Baker, L. Robertson, Mechanical properties of soft magnetic FeCo alloys. Mater. Sci. Eng. A **329**, 325–333 (2002)
66. J.A. Ashby, H.M. Flower, R.D. Rawlings, Gamma phase in an Fe–Co–2%V alloy. Met. Sci. **11**(3), 91–96 (1977)
67. B.D. Cullity, C.D. Graham, *Introduction to Magnetic Materials* (Wiley, Hoboken, 2011)